DTIC COPY

REPORT DOCUMENTATION PAGE

Form Approved
OMB No. 0704-01-0188

PLEASE DO NOT RETURN YOUR FORM TO THE ABOVE ADDRESS.

1. REPORT DATE *(DD-MM-YYYY)*	2. REPORT TYPE	3. DATES COVERED *(From - To)*
20-07-2007	REPRINT	

4. TITLE AND SUBTITLE

A Characterization of Cirrus Cloud Properties That Affect Laser Propagation

5a. CONTRACT NUMBER

5b. GRANT NUMBER

5c. PROGRAM ELEMENT NUMBER
62601F

6. AUTHORS
Donald C. Norquist
Paul R. Desrochers
Patrick J. McNicholl
John R. Roadcap

5d. PROJECT NUMBER
1010

5e. TASK NUMBER
OT

5f. WORK UNIT NUMBER
A1

7. PERFORMING ORGANIZATION NAME(S) AND ADDRESS(ES)

Air Force Research Laboratory RVBYA
29 Randolph Road
Hanscom AFB, MA 01731-3010

8. PERFORMING ORGANIZATION REPORT NUMBER
AFRL-RV-HA-TR-2008-1050

9. SPONSORING/MONITORING AGENCY NAME(S) AND ADDRESS(ES)

10. SPONSOR/MONITOR'S ACRONYM(S)
AFRL/RVBYA

11. SPONSOR/MONITOR'S REPORT NUMBER(S)

12. DISTRIBUTION/AVAILABILITY STATEMENT
Approved for Public Release; distribution unlimited.

13. SUPPLEMENTARY NOTES
Reprinted from *Journal of Applied Meteorology and Climatology*, Vol. **47**, pp 1322-1336

14. ABSTRACT Future high-altitude laser systems may be affected by cirrus clouds. Laser transmission models were applied to measured and retrieved cirrus properties to determine cirrus impact on power incident on a target or receiver. A major goal was to see how well radiosondes and geostationary satellite imagery could specify the required properties. Based on the use of ground-based radar and lidar measurements as a reference, errors in cirrus-top and cirrus-base height estimates from radiosonde observations were 20%--25% of geostationary satellite retrieval errors. Radiosondes had a perfect cirrus detection rate as compared with 80% for satellite detection. Ice water path and effective particle size were obtained with a published radar-lidar retrieval algorithm and a documented satellite algorithm. Radar-lidar particle size and ice water path were 1.5 and 3 times the satellite retrievals, respectively. Radar-lidar-based laser extinction coefficients were 55% greater than satellite values. Measured radar-lidar cirrus thickness was consistently greater than satellite-retrieved thickness, but radar-lidar microphysical retrieval required detection by both sensors at each range gate, which limited the retrieval's vertical extent. Greater radar-lidar extinction and greater satellite-based cirrus thickness yielded comparable optical depths for the two independent retrievals. Laser extinction-transmission models applied to radiosonde-retrieved cirrus heights and satellite-retrieved microphysical properties revealed a significant power loss by all models as the laser beam transits the cirrus layer. This suggests that cirrus location is more important than microphysics in high-altitude laser test support. Geostationary satellite imagery may be insufficient in cirrus detection and retrieval accuracy. Humidity-sensitive radiosondes are a potential proxy for ground-based remote sensors in cirrus detection and altitude determination.

15. SUBJECT TERMS
Cirrus cloud retrieval Laser transmission Optical thickness Radiosonde optical depth retrieval

16. SECURITY CLASSIFICATION OF:			17. LIMITATION OF ABSTRACT	18. NUMBER OF PAGES	19a. NAME OF RESPONSIBLE PERSON
a. REPORT	b. ABSTRACT	c. THIS PAGE			Donald C. Norquist
UNCL	UNCL	UNCL	UNL	10	19B. TELEPHONE NUMBER *(Include area code)*

A Characterization of Cirrus Cloud Properties That Affect Laser Propagation

DONALD C. NORQUIST, PAUL R. DESROCHERS, PATRICK J. MCNICHOLL, AND JOHN R. ROADCAP

Battlespace Environment Division, Space Vehicles Directorate, Air Force Research Laboratory, Hanscom Air Force Base, Massachusetts

(Manuscript received 10 April 2007, in final form 20 July 2007)

ABSTRACT

Future high-altitude laser systems may be affected by cirrus clouds. Laser transmission models were applied to measured and retrieved cirrus properties to determine cirrus impact on power incident on a target or receiver. A major goal was to see how well radiosondes and geostationary satellite imagery could specify the required properties. Based on the use of ground-based radar and lidar measurements as a reference, errors in cirrus-top and cirrus-base height estimates from radiosonde observations were 20%–25% of geostationary satellite retrieval errors. Radiosondes had a perfect cirrus detection rate as compared with 80% for satellite detection. Ice water path and effective particle size were obtained with a published radar–lidar retrieval algorithm and a documented satellite algorithm. Radar–lidar particle size and ice water path were 1.5 and 3 times the satellite retrievals, respectively. Radar–lidar-based laser extinction coefficients were 55% greater than satellite values. Measured radar–lidar cirrus thickness was consistently greater than satellite-retrieved thickness, but radar–lidar microphysical retrieval required detection by both sensors at each range gate, which limited the retrievals' vertical extent. Greater radar–lidar extinction and greater satellite-based cirrus thickness yielded comparable optical depths for the two independent retrievals. Laser extinction–transmission models applied to radiosonde-retrieved cirrus heights and satellite-retrieved microphysical properties revealed a significant power loss by all models as the laser beam transits the cirrus layer. This suggests that cirrus location is more important than microphysics in high-altitude laser test support. Geostationary satellite imagery may be insufficient in cirrus detection and retrieval accuracy. Humidity-sensitive radiosondes are a potential proxy for ground-based remote sensors in cirrus detection and altitude determination.

1. Introduction

Cirrus clouds are composed of varying densities of ice crystals of a variety of shapes and sizes. As light passes through the suspended layers of ice crystals, some is scattered over a range of directions and some is absorbed. The fraction of the original light exiting the cloud is of interest in determining levels of incoming solar radiation, or the light levels from stars in nighttime observations of the galaxy. Another application for determining the transmissive properties of cirrus clouds is computing the loss of power of laser light directed through the cloud layer. Lasers operating in the atmosphere are envisioned for use in high-bandwidth communications (Fischer et al. 2004) and in missile defense (Barton et al. 2004). It is important to assess the effects that cirrus clouds may have on these laser systems so that their expected performance can be determined.

Determination of the location and coverage of cirrus continues to be a daunting task in both nowcasts and forecasts. Knowing the full extent of thin or subvisual cirrus is extremely problematic, because of the sensitivity of remote sensing required for their detection. Wylie and Menzel (1999) found a 34% probability of cloud above 6 km detected from polar-orbiting satellites between 65°N and 65°S latitude. Yet their statistics do not account for undetected cirrus, which are sure to be even more spatially extensive. Temporal and spatial prevalence of cirrus indicates a need to quantify the impact that they may have on high-altitude laser systems.

Several studies have examined the effect that typical cirrus cloud properties might have on high-altitude laser transmission. Koenig et al. (1993) analyzed the potential impact of cirrus on laser propagation by modeling the transmission through cirrus properties assumed for distinct altitude layers. Cirrus extinction was derived based on the assumption of spherical ice particles.

Corresponding author address: Donald C. Norquist, AFRL/RVBXS, 29 Randolph Rd., Hanscom AFB, MA 01731-3010.
E-mail: AFRL.RVB.PA@hanscom.af.mil

DOI: 10.1175/2007JAMC1756.1

They found that the laser power loss in long pathlengths depended on the assumed cirrus extinction when the laser is directed nearly horizontally. Liou et al. (2000) demonstrated a laser transmission model applicable to near-infrared wavelengths in hypothetical scenarios involving thin cirrus clouds with specified optical properties. They computed direct and multiple-scattered transmission from source to target through a specified cirrus layer and found that transmission to the target from multiple scattering was negligibly small. Transmitted energy was found to depend upon the source–target pathlength, the cirrus optical depth, and the altitude of the cloud with respect to the source. Ou et al. (2002, hereinafter Ou02) expanded the laser transmission model to two dimensions (vertically oriented plane), allowed for inhomogeneity of cirrus structure in the cross section, and included the computation of backscattered laser power. They showed that uncertainty in laser transmission is less dependent on errors in the specified particle size distribution than on optical depth. Using typical properties for thin cirrus (optical depths < 0.5), they found that backscattered power was about four orders of magnitude less than the direct transmission power and depended on assumed crystal shape. Direct transmission varied between 1% and 50% of the source power as a function of target altitude depending on the assumed cirrus optical depth. The directly transmitted power for the inhomogeneous cloud differed significantly from the homogeneous cloud only within the cloud layer itself. Finally, the use of spherical geometries, allowing for earth curvature in the cirrus banding, had an appreciable effect on direct transmission for long pathlengths of 100 km or more even if the source and target were both 0.5 km above the cirrus top.

In the present study properties retrieved from actual cirrus measurements are used to compute laser transmittance (fraction of source power) as a function of target or receiver range and altitude. The motivation was to provide guidance to high-altitude laser system designers based on observations of actual cirrus events. Instrumentation included a ground-based cloud profiling radar and lidar, radiosondes, and satellite imagery from the the National Oceanic and Atmospheric Administration's *Geostationary Operational Environmental Satellite-12* (*GOES-12*). Without in situ ice crystal measurements available, the goal was to see if cirrus measurements from radiosondes and satellite imagery could be used as a proxy for active remotely sensed measurements in specifying cirrus properties required for computing laser transmittance.

This project involved two major tasks. The first was to specify the cirrus properties needed for the laser transmittance calculations from the raw measurements. The second was to use these property values in a laser transmission model to estimate the effect of cirrus on laser power incident on a target or receiver. The next section describes the methods employed to perform these two tasks. This is followed by a description of the data collected to retrieve cirrus properties for each event. Next, the results of the cirrus property retrievals and the laser transmittance calculations are presented. Last, the results are summarized and implications of these results are discussed.

2. Method

Atmospheric transmittance (T_s) is the fraction of light source power remaining after transit of distance s through a homogenous medium with extinction coefficient β_e:

$$T_s = \exp(-\beta_e s).$$

In laser transmission models, the extinction coefficient is computed for discrete computational layers Δz based on the atmospheric conditions. In each computational layer, the extinction coefficient includes contributions from scattering and absorption of light by constituent gases (β_{air}), by aerosols (β_{aer}), and in cloudy layers by cloud particles (β_{cld}). The optical depth for an atmospheric layer is the product of the extinction coefficient and the layer thickness. If β_{cld} is specified in each cloudy computational layer, cloud optical depth can be computed as

$$\tau_c = \Delta z \sum_{j=k_{\text{bot}}}^{k_{\text{top}}} \beta_{\text{cld}_j},$$

in which k_{bot} and k_{top} are the indices of the bottommost and topmost cloud computational layers. The laser path from airborne source to a target or receiver is discretized into path segments Δs. Taking into account the spherical geometry of the earth, the altitude of each path segment interval s_i is computed. Then the total extinction coefficient β_e for each segment interval is identified from the corresponding computational layer and the total path optical depth is computed as

$$\tau_s = \sum_{i=1}^{N-1} 0.5(\beta_{e_i} + \beta_{e_{i+1}})(s_{i+1} - s_i)$$

for N path segment intervals. Transmittance for the total path is then

$$T_s = \exp(-\tau_s).$$

The contributions to total extinction due to the "clear sky" conditions, represented by β_{air} and by β_{aer}, were

computed using the Fast Atmospheric Signature Code (FASCODE) laser transmission model (Clough et al. 1986). FASCODE was executed with a laser wavelength of 1.315 μm (following Ou02) in 20-m computational layers. The absorption and scattering of light due to air molecules assumes a climatology of constituent gases (Anderson et al. 1986). The radiosonde relative humidity determined water vapor concentration in each layer. Attenuation due to aerosols is due to scattering and absorption of the laser light, primarily in the planetary boundary layer. The aerosol climatology profile is taken from the Air Force Research Laboratory (AFRL) low-resolution transmittance model and code (LOWTRAN) (Kneizys et al. 1988) "rural" aerosol model.

Three laser transmission models of extinction due to ice particles were utilized only in cloudy computational layers. This was done to appreciate the degree of uncertainty among algorithms ranging from simple to complex, and no attempt was made to validate the results. The first model, as described by Bohren and Huffman (1983), applies Mie theory in assuming spherical ice particles in a modified gamma size distribution. A second estimate of cirrus extinction was generated from the parameterization by Fu (1996, hereinafter Fu96). These algorithms require that ice water content (IWC) and effective particle size (D_{eff}, ratio of the integrated particle volume to area) be specified, and return an estimate of the cirrus extinction coefficient for a specific optical wavelength. Bulk (cirrus-layer mean) values of IWC and D_{eff} were used in each computational layer for laser transmittance calculations to compute β_{cld}. They were also applied in each of the cloudy computational layers to compute cirrus optical depth.

The third laser transmission model considered was that of Ou02. Though their model computes β_{air} and β_{aer} in each computational layer, this was disabled in favor of the FASCODE computation. The model requires that the bulk β_{cld} and D_{eff} be specified and estimates the direct, forward scattered, and backscattered power at the base of each computational layer. The bulk β_{cld} as estimated by the Fu96 algorithm is used along with the bulk D_{eff} satellite retrieval. The change in computed power between sequential computational layer bases was converted to optical depth for the intervening layer. Dividing this by the path through each layer yields the cirrus extinction for the layer. Following Ou02, a laser wavelength of 1.315 μm and a laser source power of 1 Mw was used in the calculations.

The extinction coefficient computed from the Mie, Fu96, and Ou02 models for each cloudy computational layer was added to the FASCODE clear-sky extinction for the layer to determine the total computational layer extinction β_e according to each model. These were used to compute the transmittance for the source–target/receiver path as described above. Total path transmittance was computed for each 20-m altitude increment of a target or receiver rising vertically from a launch point at a specified earth surface separation distance from a point directly below the airborne laser source.

In this study horizontal homogeneity of the required conditions is assumed within the range of source–target separation distances considered. Therefore, a single profile of the atmospheric state and the cirrus characteristics are used in the laser transmittance calculations. While the atmospheric state and cirrus characteristics can vary significantly over distances of laser transit, a one-dimensional specification of the observed atmospheric conditions should give at least a representative estimate of their potential impact on laser propagation in the region.

3. Data

Field measurements were made at Hanscom Air Force Base, Massachusetts (42.455°N, 71.271°W) on 26 selected dates in 2005. The criteria for commencing measurements were broken or overcast cirrus overhead expected to last at least 3 h with no more than scattered lower clouds. A ground-based lidar and radar began measurements when the sky condition criteria were met. Detection of a return from cirrus by the ground-based lidar marked the beginning of the minimum 3-h observing period. A radiosonde was launched after at least 30 min of cirrus detection by the radar.

The Air Force Cloud Profiling Radar (AFCPR) is a 35-GHz (8.6 cm) Ka-band radar (Desrochers 2004) designed to provide reflectivity measurements to -40 dBZ at 75-m range intervals from all cloud types except those with the smallest particle sizes (e.g., shallow cumulus). It operates with a peak power of 1.6 kW and for this project performed cirrus sensing with an average power of 6.5 W and 4-kHz pulse repetition frequency. The Portable Electronic Eyesafe Laser System (PEELS) is a small direct-detection lidar that operates at 1.574 μm and 20-Hz pulse repetition frequency to measure backscattered power from detectable targets. It transmits with a signal power of 0.6 W. AFCPR and PEELS measurements were averaged for 1 and 10 s, respectively, for analysis purposes. These two ground-based remote sensors are hereinafter referred to as radar and lidar in this paper.

The radar and lidar have complementary capabilities in cirrus detection. The shorter wavelength lidar is more sensitive to cirrus particles and can usually measure base, and top of transmissive cirrus, more accurately than the radar. However, lidar is more subject to attenuation (though only slightly more so than visible

light), whereas the radar can usually penetrate optically thick cirrus and determine their top altitude. In addition, PEELS produces a polarization ratio = depolarized power/polarized power: spherical particles (droplets) have a value near zero and irregular particles (crystals) a larger value. This information helps determine water phase in the cloud layer to assure that only ice clouds were included in the present study.

Top and base cirrus-layer edges detected by the near-zenith copointing radar and lidar provided reference measurements of cloud-top altitude (CTA) and cloud-base altitude (CBA). The higher of the radar and lidar top and the lower of the radar and lidar base were used. IWC and effective particle radius r_{eff} were retrieved from measurement profiles through the cirrus layer utilizing the algorithm of Donovan and van Lammeren (2001). Their scheme is one of several remote sensor cirrus property retrieval algorithms reviewed by Comstock et al. (2007). The scheme was modified to account for the lidar and radar wavelengths, but the particle size distribution specification as a gamma function of width parameter 5 was maintained. The algorithm was operated in single scattering mode and was only applied in observing periods involving ice clouds. Donovan and van Lammeren (2001) estimated uncertainties of 25%–60% for IWC and 5%–10% for r_{eff} in pure ice retrievals (as deduced from their Fig. 17). Measurements of CTA and CBA by the radar and lidar and retrievals of IWC and r_{eff} presented in the next section are referred to as the "R/L" values.

Soundings of pressure, temperature, and relative humidity were taken with balloon-borne Vaisala model RS92-SGP radiosondes at 1–2-s intervals. Altitude and wind speed and direction are determined using a global positioning system receiver. Of particular relevance to this project are the dual thin film capacitor humidity sensors that allow one sensor to be heated to evaporate condensed water while the other is taking measurements. Relative humidity (with respect to saturation mixing ratio over an ice surface, RH_i) was derived from pressure, temperature, and relative humidity (with respect to saturation mixing ratio over a liquid surface, RH_l) measurements.

At altitudes between CBA and CTA as determined by combined radar and lidar measurements, RH_i was significantly greater than RH_l and exhibited strong relative maxima in the sounding. Other investigators (e.g., Wang and Rossow 1995; Chernykh and Eskridge 1996) have developed empirical methods to estimate cloud-layer boundaries from radiosonde profiles. Because they are empirical methods, their performance is sensitive to the differences in radiosonde humidity sensors and vertical resolution of the data (Seidel and Durre 2003). In the current project, cloud probability (CP, likelihood of cloud presence at a radiosonde report level) was diagnosed from radiosonde relative humidity (RH). Nonlinear CP = f(RH) empirical relationships were developed from lidar and radar cloud-base and cloud-top measurements and radiosonde soundings from past cloud observation campaigns. The development of these relationships is summarized in the appendix. Estimates of CTA and CBA described in the next section derived from the CP = f(RH) relationships applied to this project's radiosonde observations are referred to as the raob values.

Satellite imagery data were obtained from the Air Force Research Laboratory ground station downlink from the *GOES-12* satellite. Imagery channels of 0.65, 3.9, 6.75, and 10.7 μm are utilized in the cloud detection and property retrieval (CDPR; Gustafson and d'Entremont 2000) to discriminate cloud from background brightness temperatures and determine cloud water phase. In ice cloud picture elements (pixels), effective temperature and 10.7-μm emissivity are simultaneously retrieved. Effective temperature of the detected ice cloud is the temperature of the radiative center of mass of the cloud layer. Upon imposing assumptions about the particle size distribution, estimates of ice water path, visible optical depth, and effective particle size are obtained. Temperature and height of pressure surfaces from postprocessed Air Force Weather Agency fifth-generation Pennsylvania State University–National Center for Atmospheric Research Mesoscale Model (MM5) forecasts interpolated to the image time provided a cloud-top altitude assignment from the effective temperature. Cloud-base altitude was specified assuming a default cirrus thickness of 1100 m. A celestial dome of radius 28 km centered on the radiosonde launch site was estimated based on a nominal cirrus altitude of 10 km and ground clutter leading to minimum above-horizon viewing angle of 20°. CTA, CBA, IWP, and D_{eff} in all ice cloud pixels within this viewing region were averaged to represent the satellite-retrieved cirrus characteristics. This removes spatial resolution differences between single-pixel satellite retrievals and reference radar–lidar measurements as cirrus crossed the celestial dome. Spatially averaged cirrus property retrievals from the *GOES-12* imagery using the CDPR algorithm, as presented in the next section, are referred to as the "GOES" retrievals.

Table 1 lists the 28 raobs taken over the 26 observing periods. Also shown are the observing times for the radar and lidar, the GOES imagery time, and the causative mechanism for the cirrus event over eastern Massachusetts. Twenty-six cases in 11 months do not capture the full range of variability of midlatitude cirrus

TABLE 1. Hanscom Research Site cirrus cloud field experiment measurements in 2005. All times are UTC.

Date	Raob launch time	R/L obs period	GOES image time	Cause of Ci
17 Feb	1526	1500–1800	1545	Front
24 Feb	1656	1200–1900	1645	Jet stream
22 Apr	1453	1410–1800	1515	Front
06 May	1145	1100–1400	1145	Front
20 May	1156	1100–1500	1215	Front
20 May	1353	1100–1500	1415	Front
03 Jun	1346	1200–1600	1415	Front
21 Jun	1505	1400–1710	1515	Jet stream
24 Jun	1401	1250–1620	1415	Jet stream
21 Jul	1656	1600–1900	1715	Convection
26 Jul	1602	1505–1805	1615	Front
29 Jul	1331	1240–1830	1345	Front
29 Jul	1644	1240–1830	1715	Front
08 Aug	1245	1155–1500	1315	Front
16 Aug	1556	1507–1812	1615	Jet stream
18 Aug	1146	1100–1400	1215	Front
19 Aug	1420	1125–1525	1445	Front
26 Aug	1416	1320–1620	1445	Front
09 Sep	1149	1055–1237	Missing	Front
30 Sep	1135	1040–1515	1145	Jet stream
19 Oct	1232	1140–1445	1245	Jet stream
20 Oct	1339	1255–1600	1345	Jet stream
21 Oct	1730	1410–1930	1740	Front
31 Oct	1229	1145–1500	1245	Jet stream
01 Nov	1914	1655–2030	1945	Front
09 Nov	1300	1135–1500	1315	Front
05 Dec	1611	1515–1820	1615	Jet stream
22 Dec	1514	1420–1720	Missing	Jet stream

conditions, but allow for testing the capability of retrieval techniques in their seasonal variation.

4. Results

a. Cirrus property retrievals

Location and prevalence of cirrus are first-order characteristics in regards to their effect on laser transmission. Cirrus-top height accuracy is crucial in the assignment of laser source altitude so that a laser path may avoid ice crystal layers. Figure 1 shows a comparison of the cirrus-top altitudes as retrieved from the satellite imagery, the radiosonde relative humidity, and as measured by the radar and lidar. Also shown is the tropopause altitude as determined from the raob using the algorithm of Roe and Jasperson (1980). The *GOES-12* CDPR algorithm has a tendency to understate the CTA. The empirical CP = f(RH) algorithm applied to the raobs, especially when limited by the tropopause height, achieves a better match in CTA with the radar–lidar measurements. The raob-diagnosed CTA also more closely follows the case-to-case variation of the radar–lidar values. Raobs diagnosed the presence of cirrus overhead in all cases while the satellite-based cloud detection scheme failed to detect cirrus overhead in five cases.

CBA retrievals and measurements are shown in Fig. 2. There appears to be a tendency of the GOES retrievals to be too high. The raob-based CBA retrievals show even greater accuracy than the corresponding CTA values. This is seen in a comparison of statistics over all cases as shown in Table 2. Bias, mean absolute error, and standard deviation of the error statistics, when evaluated against radar–lidar values as reference, are shown for the GOES and raob retrievals for just the cases detected by the satellite and for the raob retrievals for all cases. For the raob estimate, CTA mean absolute error is about 1.6 times that of CBA, and would be an even greater error if CTA was not tropopause constrained. Because of uncertainties in time selected to evaluate the radar–lidar signal for CTA and CBA for these comparisons and because of range gate resolution, the specification error of radar–lidar CTA and CBA is estimated to be ±200 m. Clearly the CBA estimate from the raob retrieval is competitive with this error of estimate and suggests the absence of any systematic error.

The statistics for retrieved cirrus thickness indicate that the raob estimates result in layers diagnosed too thin by an average of 0.4–0.5 km, compared to GOES negative thickness bias of 1.8 km. Clearly the in situ sensor of the radiosonde, while not measuring cloud properties directly, has an advantage over the remotely sensed vertical cloud boundaries by the satellite sensors. This is especially true of the cloud base that is undetected by the satellite.

Laser transmission calculations require IWC and the D_{eff}. While the retrieval algorithm of Donovan and van Lammeren (2001) applied to the radar and lidar measurements can produce their profiles, the CDPR algorithm of Gustafson and d'Entremont (2000) applied to *GOES-12* imagery provides only bulk values for each pixel. The CDPR algorithm retrieves ice water path (IWP), D_{eff}, CTA, and CBA. Cirrus-layer-mean IWC is computed from IWP/(CTA − CBA). The radar–lidar cirrus retrieval algorithm can only produce IWC and r_{eff} values for portions of the cirrus layer detected by both the radar and lidar. For this purpose, the highest base and lowest top detected by the radar–lidar tandem act as the CBA and CTA defining the vertical domain of the retrieved IWC and r_{eff} values. This underestimates the full thickness of the cirrus layer in comparison to using the highest top and lowest base as depicted in Figs. 1 and 2.

Retrieved particle size comparisons require a recon-

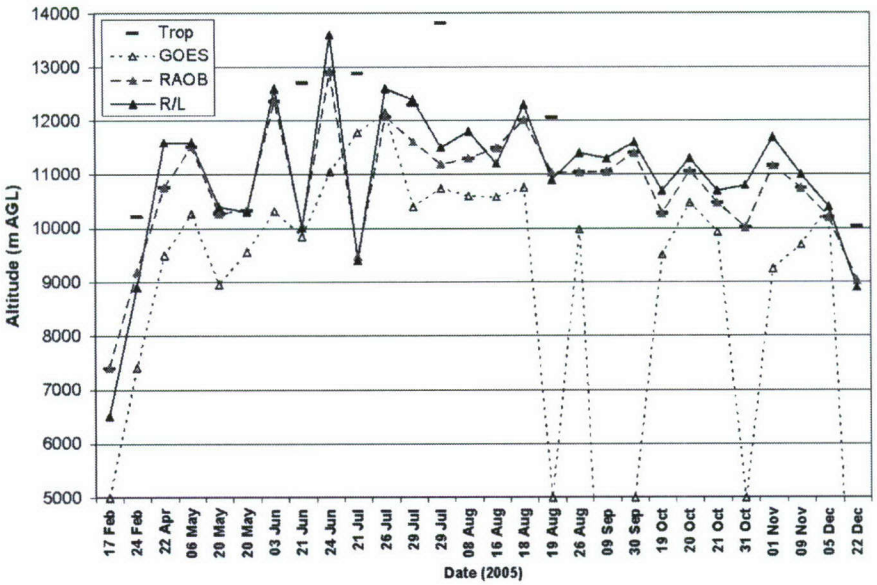

FIG. 1. Cloud-top altitudes retrieved from GOES imagery (undetected shown as 5000 m) and from raob relative humidity, as compared with radar and lidar (R/L) measurements. Tropopause (Trop) altitude is determined from the raob in each case.

ciliation of definitions. Gustafson and d'Entremont (2000) define D_{eff} as the ratio of the third and second moments of the size distribution of ice crystal diameter, taken as the long axis dimension. Donovan and van Lammeren (2001) use the same ratio for effective radius r_{eff} but specify the radius of an equivalent sphere. For the same moment ratios, $D_{\text{eff}} = 2r_{\text{eff}}$ (McFarquhar and Heymsfield 1998) but only if the same particle dimension is assumed. In this case, $D_{\text{eff}} > 2r_{\text{eff}}$ for a given size distribution because the maximum particle dimension is generally greater than the diameter of a sphere of equivalent volume. So the CDPR retrievals represent a somewhat larger particle than the R/L retrievals.

Table 3 compares CDPR-retrieved and R/L-re-

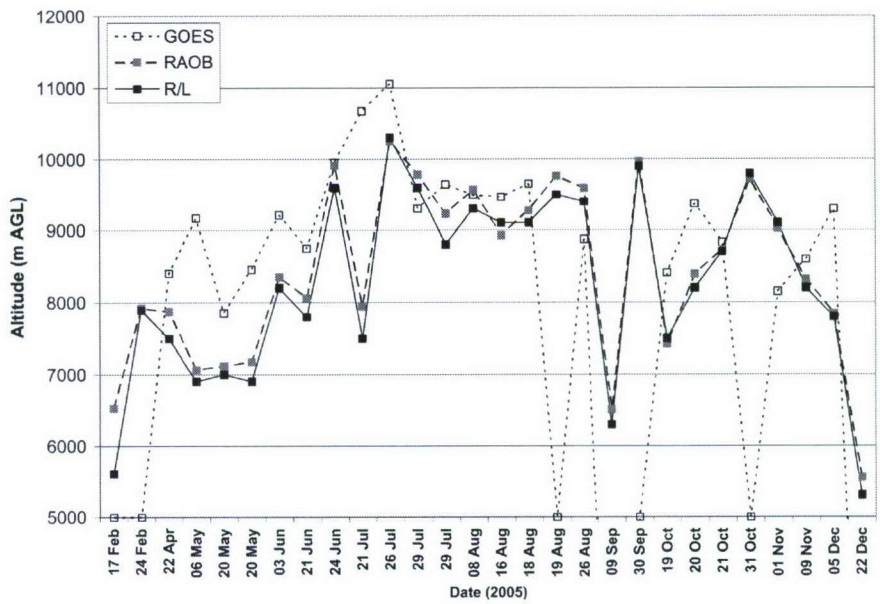

FIG. 2. As in Fig. 1, but for retrieved (GOES, raob) and measured (R/L) cloud-base altitudes.

TABLE 2. Statistics from the comparison of the diagnosis of cloud-top height, cloud-base height, and consequent depth of the observed cirrus layer as retrieved from GOES and raob data with corresponding AFCPR–PEELS radar–lidar cirrus-layer measurements. Statistics include bias, mean absolute error (MAE), and std dev of the error. Values are shown for the 21 cases in which CDPR detected cirrus as shown in Figs. 1 and 2, and for all 28 observing periods. All units are meters.

	Cirrus-layer top			Cirrus-layer base			Cirrus-layer depth		
	Bias	MAE	Std dev	Bias	MAE	Std dev	Bias	MAE	Std dev
GOES-12	−1086	1312	1071	767	936	909	−1852	1852	816
Raob-21	−294	336	288	159	196	169	−454	498	353
Raob-28	−212	348	378	179	213	215	−391	444	355

trieved cirrus-layer-mean (bulk) particle sizes and ice water path for all-ice cloud-observing periods. As shown by Comstock et al. (2007), such algorithms can produce a significant range of values for a given case, so the values shown should be taken as specific to the algorithms used with the understanding that some degree of uncertainty exists. For comparison purposes, the retrieved R/L r_{eff} and IWC range gate values were vertically averaged at each retrieval time (approximately 30-s intervals) during the 10 min following the Table 1 *GOES-12* image time. The vertical averages were temporally averaged for comparison with the bulk GOES CDPR retrievals. Finally, the r_{eff} estimates were doubled (to approximate D_{eff}) and the IWC was multiplied by the time-averaged vertical depth of the retrieved values (to approximate IWP). Table 3 shows that the R/L particle size retrievals are larger by an average factor of 1.5 and more temporally variant than the GOES retrievals. R/L IWP estimates are larger than GOES estimates by an average factor of 3. Since a larger IWP increases extinction while a larger D_{eff} decreases extinction, the ice mass and particle size differences should counteract each other somewhat in the extinction computations for the two sets of retrievals.

b. *Laser transmission calculations*

As mentioned in the introduction, the second major objective of this project was to use the retrieved cirrus properties in laser transmission models to determine cirrus effects on laser propagation. The three laser transmission models considered were described in section 2, along with the utilization of the GOES-retrieved ice mass and particle size. The raob-retrieved cirrus depth was used to indicate cloudy computational layers in the sounding due to its improved accuracy over the GOES cirrus depth.

The vertical cirrus optical depth obtained from the Mie, Fu96, and Ou02 (both direct transmission and total power = direct + forward scattered) transmission models are shown in Fig. 3 for all cases in which the GOES–CDPR algorithm detected cirrus. Also shown is the cloud depth from the raob retrievals of CTA and CBA. The figure shows that the vertical cirrus optical depth differs less among the transmission models than the difference from case to case.

Without exception, the Ou02 model optical depths are less than those from the Mie and Fu96 algorithms. The difference is greater with increasing cirrus optical depth. This is due to the fact that the same bulk extinction value was imposed in all cloudy computational layers in employing the Mie- and Fu96-derived cirrus extinction, whereas the Ou02 laser transmission model calculated a value of cirrus extinction for each computational layer. Ou02 modify the extinction coefficient by a term accounting for effects of delta-function transmission (Takano and Liou 1989) that reduces extinction depending on the layer's scattering constituents. The Ou02 cirrus extinctions actually decreased with decreasing laser power during the laser's transit through the cirrus, explaining why the Ou02 versus Mie– Fu96

TABLE 3. A comparison of the retrieved values of r_{eff} (converted to D_{eff}; μm) and IWC (converted to IWP; g m^{-2}) from the R/L cirrus measurements, with IWP and D_{eff} retrievals from *GOES-12* imagery for observing periods in which significant amounts of liquid clouds were not detected by the lidar. Radar–lidar values represent the vertical and time average of all nonzero retrieved IWC and r_{eff} values in the cirrus layer in the 10-min period beginning at the satellite image time are indicated.

Date/time (UTC)	GOES D_{eff}	R/L r_{eff} × 2	GOES IWP	R/L IWC × Δz
17 Feb/1545	0	58.78	0	16.41
22 Apr/1515	45.96	78.52	9.07	52.82
6 May/1145	44.01	76.14	24.04	70.19
20 May/1215	46.13	76.96	20.93	67.87
20 May/1415	49.98	95.24	29.21	122.20
21 Jun/1515	49.51	90.70	25.42	83.91
24 Jun/1415	45.23	59.00	12.99	26.51
26 Jul/1615	44.61	63.66	10.73	42.34
8 Aug/1315	47.20	83.82	21.22	83.06
31 Oct/1245	0	50.48	0	11.47
1 Nov/1915	45.35	56.24	13.05	22.55
9 Nov/1315	46.09	73.42	16.05	48.87
5 Dec/1615	46.26	62.98	11.60	37.08

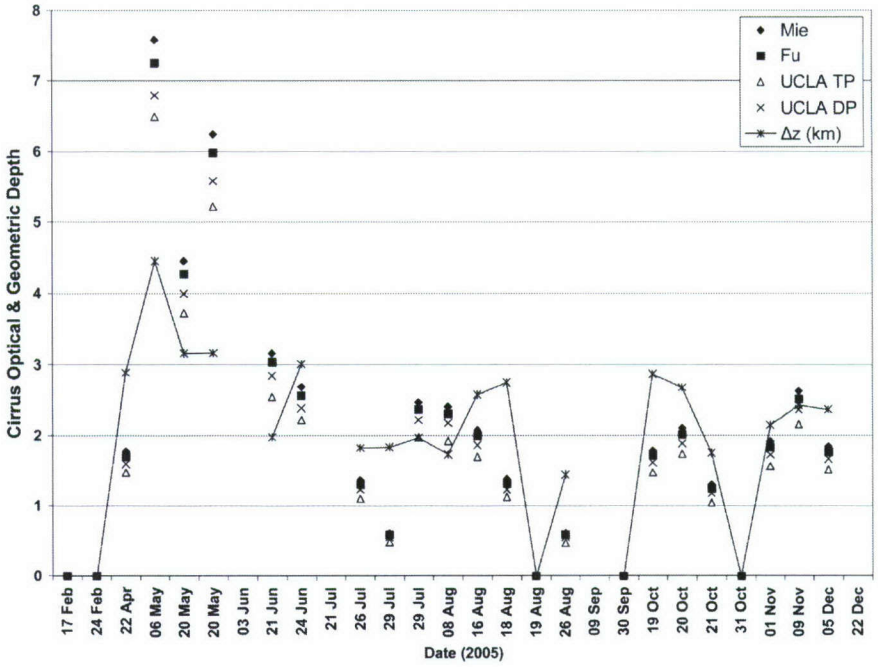

FIG. 3. Cirrus optical depth computed from Mie theory, Fu96, and Ou02 [labeled "UCLA" for both total power (TP) and direct power (DP) transmission] algorithms assuming GOES-retrieved layer-mean ice water content and effective particle size and raob-retrieved cirrus-top and cirrus-base altitude. Also shown is cirrus-layer geometric depth (Δz; km) in each case assuming raob-retrieved cirrus-top and cirrus-base altitude.

optical depth difference increases with increasing cirrus optical depth.

Figure 3 also shows that the Ou02 total power transmission always results in a lesser optical depth than the Ou02 direct power transmission. This is because the forward scattering included in the total laser power adds an additional increment of laser power (as much as 10%–15%) to the direct power in a laser beam directed vertically. As shall be shown, the forward scattering contribution is greatly lessened in nonvertical laser paths.

Vertical optical depth is not always positively related to geometric cloud depth, as seen in Fig. 3. Cirrus-layer thickness increases may be more than overcome by a decrease in the ice water content. For example, in the 8–18 August cases, IWP decreased from 21 to 8 g m^{-2} while geometric thickness increased by about 1 km, causing a decrease in optical depth. Comparing a plot of CDPR-retrieved IWP and D_{eff} (not shown) with Fig. 3 revealed that the case-to-case variation of optical depth is much more closely correlated with IWP changes than with the relatively steady D_{eff}.

Figure 4 depicts the profiles of laser transmittance experienced by an ascending vehicle launched from a point essentially underneath the laser source. The atmospheric state specification and the cirrus-layer characteristics are based on the 1416 UTC 26 August 2005 raob. As can be seen in Fig. 3, this case has the smallest vertical cirrus optical depth. It was chosen to illustrate the transmittance computation profiles for the most transmissive case.

By comparing the cirrus model curves with the clear-sky curve, it is obvious that the cirrus attenuation plays a predominant role in the total reduction of laser power for altitudes below cirrus top. While all curves are drawn from 15 km AGL to the ground, a significant departure from a transmittance of 1 is seen beginning at cirrus top. The laser transmission models indicate a reduction of 30%–40% of the originating power through cirrus scattering and absorption through the cloud layer, while the clear-sky attenuation is minimal through the layer. For points below the cloud layer, little attenuation of the laser beam occurs until the lower altitudes where aerosol concentrations are greater in the boundary layer. Mie theory and Fu96 specifications of cirrus extinction result in a greater total optical depth (thus a lesser transmittance) than the Ou02 model results. The difference between Ou02–TP and Ou02–DP is due to forward scattering increasing the power on target/receiver.

Figure 5 shows the same profiles of transmittance, except that the earth surface separation distance be-

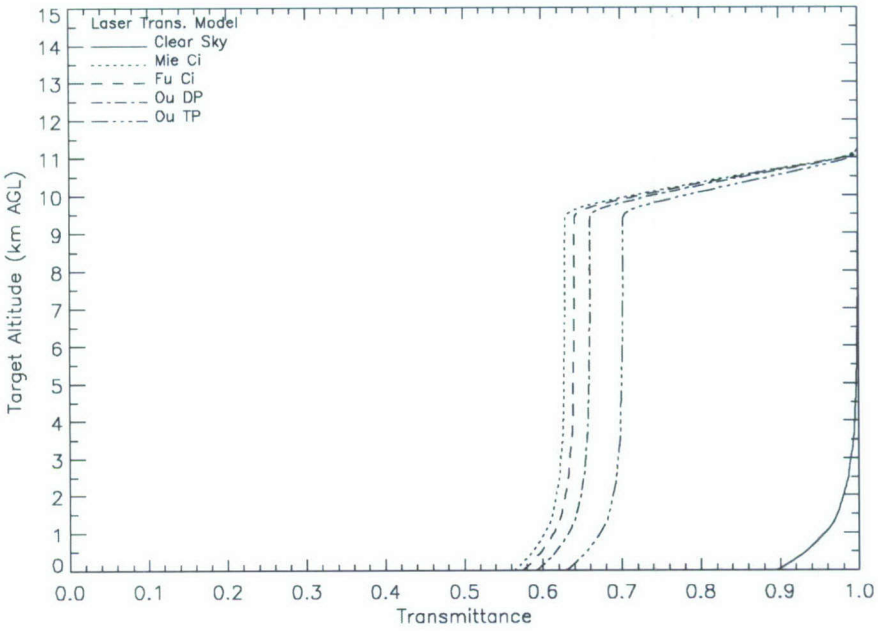

FIG. 4. Laser transmittance (fraction of original source power) received at a target or receiver as a function of target/receiver altitude for a launch point 0.01-km earth surface distance from the point over which the laser source is loitering at 11.5 km MSL (11.419 km AGL) for the different models indicated. Atmospheric state for "clear sky" (molecular and aerosol scattering and absorption) is based on a raob launched 1416 UTC 26 Aug 2005. Cirrus top and geometric depth from raob retrieval are 11.039 km AGL and 1.441 km, respectively. Cirrus ice water path and effective particle size are specified in the laser transmission models from the 1445 UTC 26 Aug 2005 *GOES-12* retrievals.

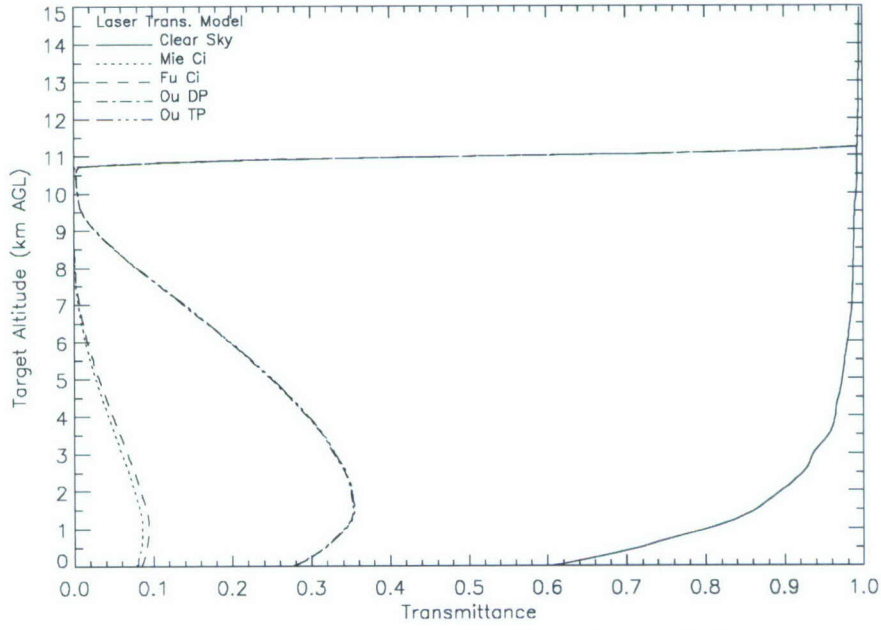

FIG. 5. As in Fig. 4, but for a 50-km earth surface distance between the laser source at 11.419 km AGL and the launch point of the ascending target/receiver.

tween source and target/receiver is 50 km. For altitudes within the cloud below about 10.7 km, virtually all power is reduced by the Mie and Fu96 algorithms, and only about 0.3% of originating power remains at the level of greatest total power loss for the Ou02 algorithms. As the laser scan angle increases directing the beam to points at lower altitude in vehicle ascent, the pathlength through the cirrus layer decreases. This reduces the cirrus attenuation and results in increasingly greater transmittances until the boundary layer aerosols are encountered. Note that the difference between Mie and Fu algorithm transmittances have decreased from Fig. 4, and the two Ou02 algorithm results are virtually indistinguishable. The latter results indicate that forward scattering effects are significantly diminished when the laser path is more off-vertical. The spherical geometry effect can be seen by comparing the altitude of first decrease of transmittance between Figs. 4 and 5. The slightly higher level of the beginning of cloud-top attenuation in Fig. 5 is the result of intercepting some portion of the cloud layer along its path even when the target/receiver is above the cloud.

The transmittance for this scenario as a function of earth surface separation distance for the Fu96 and Ou02 direct power cirrus models and clear-sky attenuation is shown in Fig. 6. The same plots for the Mie theory and Ou02 total power are not shown because of their similarity to the Fu96 and Ou02–DP plots respectively. In the absence of the cirrus layer, more than 90% of the originating laser power remains for all altitudes greater than 6 km out to a 200-km source–target/receiver separation distance. When cirrus is present, less than 10% of originating source laser power remains on the receiving vehicle positioned just below the cloud for launch distances of approximately 10 km for Mie and Fu96 algorithms and about 30 km for the Ou02 model. These 10% power distances increase with decreasing target altitude below the cloud layer down to the top of the aerosol-laden boundary layer. It is clear that appreciable laser power loss results from slant-path transit through a cirrus cloud of modest optical depth.

An efficient way to compare the expected laser extinction effect of CDPR retrievals of IWP and D_{eff} from *GOES-12* versus radar–lidar retrievals of mean IWC and r_{eff} (converted to IWP and D_{eff}) is to evaluate the resulting bulk cirrus extinction. Figure 7 is a scatterplot of the bulk cirrus extinction coefficient (β) versus the geometric depth for each case included in Table 3. The β indicated "CDPR" used the retrieved IWP and D_{eff} from satellite and raob-retrieved CTA and CBA. The β denoted as "R/L" used all of these properties as deduced from the vertical-time mean of each radar–lidar retrieval. All cirrus extinction values are computed us-

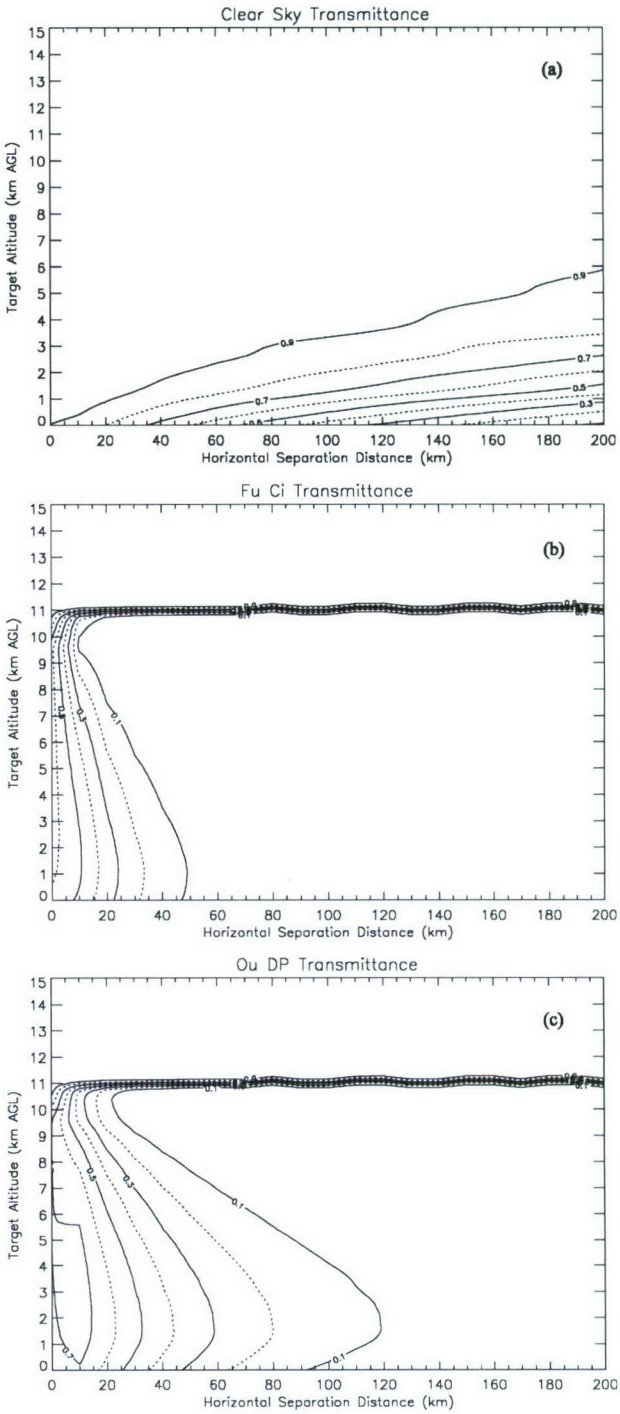

FIG. 6. Contour plots of laser power transmittance as a function of earth surface separation distance between a laser source loitering at 11.419 km AGL and the launch point of an ascending target/receiver. Atmospheric specification and cirrus properties are the same as in Fig. 5. Transmittances are shown for (a) clear sky, (b) Fu96, and (c) Ou02 direct power laser transmission models.

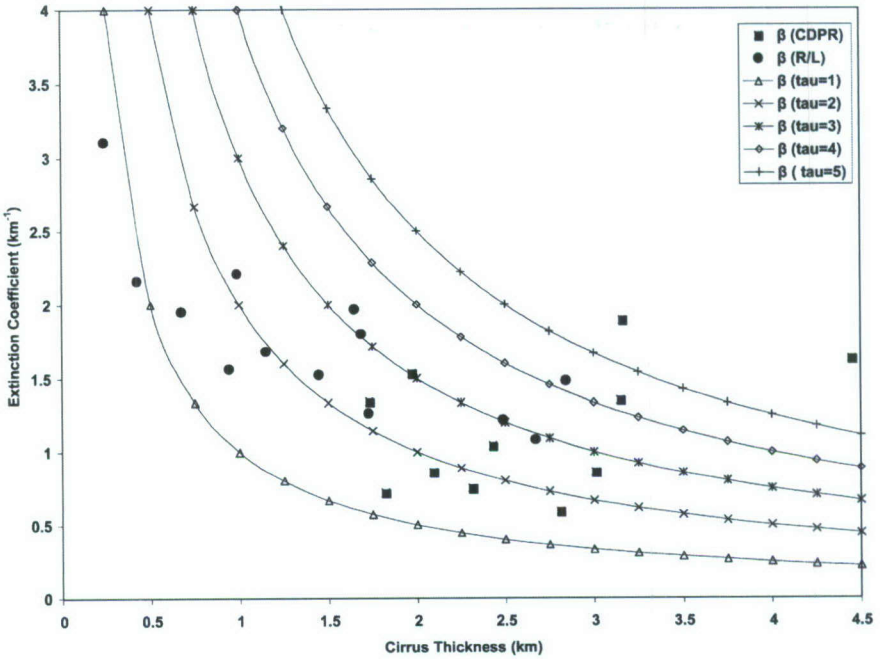

FIG. 7. Scatterplot of the cirrus extinction coefficient (km^{-1}) computed using the Fu96 algorithm applied to the GOES IWP and D_{eff} retrievals using the CDPR algorithm, and the radar–lidar (R/L) retrievals using the Donovan and van Lammeren (2001) IWC and r_{eff} retrievals (converted to mean IWP, D_{eff}) as shown in Table 3. Also shown for reference are curves of constant optical depth ("tau"), which is the product of the extinction coefficient and the cirrus-layer thickness.

ing the Fu96 algorithm. Also shown on the plot for reference are lines of constant vertical optical depth, which is the product of the extinction and the cirrus-layer geometric thickness. The R/L extinction coefficients are on average 55% greater than the CDPR-based values. The R/L cirrus thickness is reduced from its full extent (as depicted in Figs. 1 and 2) to that portion of the vertical extent detected by both radar and lidar. Therefore, radar–lidar microphysical retrievals generally result in lower geometric thicknesses than the satellite and raob-based retrievals. But the resulting vertical optical depths of the two retrieval sources are comparable. This suggests that, given the limitations of the two types of retrievals, the basis for computed impact of the cirrus on laser transmission would be similar.

5. Discussion

The major goals of this project were to obtain actual cirrus cloud properties pertinent to the transmission of laser light and to utilize them in laser transmission models. To economize high-altitude directed energy system tests, it is of interest to see if radiosondes and satellite imagery can be used as a source of the cirrus properties required in laser transmission models.

Comparison of radiosonde- and GOES-retrieved CTA and CBA with the radar/lidar reference showed that the radiosonde retrievals were considerably more accurate. While both had negatively biased CTA and positively biased CBA, the radiosonde biases were less than 30% of the satellite biases. GOES errors are likely due an underestimate of surface upwelling radiation (retrieved emissivity too large) and the use of a default geometric thickness that is too small. The radiosonde retrievals also more closely tracked the period-to-period variation of the cirrus top and base altitudes than did the GOES retrievals so that the error variance was smaller. In addition, the radiosonde algorithm detected the presence of cirrus in all 28 cases, whereas the GOES detection algorithm did not detect cirrus near the radiosonde launch site in five cases.

These results suggest that cirrus detection and property retrieval from GOES using the current algorithm may not be adequate to insure accurate specification of cirrus for laser transmission computations. Failure to detect thin cirrus may lead to laser deployment in inopportune locales. More imagery channels and higher spatial resolution, such as are available from the Moderate Resolution Imaging Spectroradiometer instrument, may provide better support for high-altitude laser operations.

Since all cases involved the presence of a cirrus layer,

no evaluation of the false-alarm rate of detection by the radiosonde algorithm was possible. But it appears that the RS92-SGP radiosondes were sensitive enough to detect cirrus missed by the geostationary satellite imagery algorithm. This as well as the relative accuracy of the radiosonde CTA and CBA retrievals suggests that they may be a suitable substitute for ground-based active remote sensors for cirrus detection and vertical positioning in support of high-altitude laser tests.

Retrievals of bulk IWP and D_{eff} from the *GOES-12* imagery were compared with vertically averaged ice water content (IWC) and r_{eff} retrievals from the radar/lidar measurements. Both IWP and D_{eff} were considerably smaller in magnitude than the corresponding radar–lidar retrievals for the compared cirrus cases. This is largely due to the majority of the irradiance sensed by the satellite sensors being emitted from the upper portion of the cirrus where particle sizes are smaller. The radar–lidar cirrus-layer-mean IWC and r_{eff} were averages from the cirrus profile detected by both sensors, which would include the lower, larger particles. Smaller IWC would reduce extinction while smaller particle sizes would increase extinction. In any case, satellite algorithm underestimates would limit the accuracy of cirrus extinction in laser transmittance computations.

IWP and D_{eff} retrievals from *GOES-12* imagery were used in three laser transmission algorithms to compute cirrus vertical optical depth at a laser wavelength. In the Mie theory and Fu96 algorithms, optical depth was the product of a computed bulk cirrus extinction coefficient and the cirrus geometric depth. In the Ou02 model, the computed optical depth was summed over all computational increments of the cirrus layer. A comparison of optical depths showed that the case-to-case variations were greater than the differences between the models. The optical depths from the Mie theory and Fu96 algorithms were consistently larger than the Ou02 optical depths, and this difference increased with optical depth. This is due to imposition of the constant cirrus extinction in each computational layer in the Mie and Fu96 algorithms, in contrast with the extinction that depends on each layer's scattering properties as computed by the Ou02 model. The Ou02 extinction actually decreased along the laser path through the cirrus as laser power decreased as a result of attenuation. Smaller optical thickness and larger transmittance are the result of the more realistic processes in the Ou02 model. The forward scattering component in the Ou02 model supplements the transmittance due to the directly transmitted laser light.

Transmittance from a high-altitude source above the cirrus layer to an ascending target or receiver was computed for each of the models and for clear sky based on the observational case with the smallest cirrus optical depth. Transmittance profiles were computed for increasing earth surface separation distances between laser source and vertically ascending target/receiver launch point out to 200 km. Results consistent with cirrus vertical optical depth computations showed that transmittance of a vertically directed laser beam was greater from the Ou02 model than from the Mie theory and Fu96 algorithms. It was even stronger when the forward scattering was included in Ou's model. Transmittance significantly decreased with increasing laser-target/receiver earth surface separation distance. Increasing slant-path distance through the cirrus layer dramatically decreases transmittance at the target/receiver. It is greater well below the cloud layer than it is at the base of the cloud for a given separation distance. Increased pathlength through the cirrus also reduces the forward scattering contribution in the Ou02 model. In all three models, laser power was reduced to about a tenth of the original power for separation distances of 30 km or greater just below the cloud and distances of 120 km or greater just above the aerosol-laden boundary layer.

These results suggest that cirrus clouds have a potentially large impact on laser transmission. They also indicate that a physically based laser transmission model is required to realistically simulate expected laser extinction. Inaccuracy of satellite-based microphysical retrievals limits the precision of laser transmission computations. However, even with the uncertainty in the ice cloud property specifications and the differences in the laser transmission models, a clear consensus for the effect of cirrus on laser propagation emerges from this study. Since the optically thinnest cirrus case revealed a large impact, it appears that a knowledge of location of the cirrus with respect to the laser source and the target/receiver vehicle is more important than knowing the microphysical properties. In fact, very thin cirrus undetected by the GOES algorithm may pose an impediment to high-altitude laser operation. Specification of the location and coverage of a cirrus layer is crucial to the deployment of a laser source to assure cirrus avoidance and to insure its effectiveness in tests or operations. Radiosondes sensitive to moisture variations in the upper troposphere could provide a level of cirrus detection capability useful in support of high-altitude laser activities. More evaluation of their cirrus-detecting ability should be conducted to ascertain the risks of using them in place of ground-based remote sensors.

Acknowledgments. The authors express their appreciation to the following people for their contribution to

the cirrus characterization project: radar operations—Kris Robinson, Jonathan Blanck, and Taylor Harrell; lidar measurements and analysis—Mitch Laird; radiosonde observations—George Clement; satellite imagery analysis—Gary Gustafson, Bob d'Entremont; FASCODE software adaptation—Jim Chetwynd; laser transmission model code—Steve Ou. This work was funded by the 6.2 applied research program of the Air Force Research Laboratory.

APPENDIX

An Empirical Method to Deduce Cloud Probability in a Radiosonde Sounding

Radiosonde observations provide accurate soundings of pressure, temperature, humidity, and winds for characterization of the atmospheric state. However, they do not make explicit measurements of cloud properties. An empirical algorithm was devised to take advantage of the high precision in situ data from raobs in estimating the vertical boundaries of cloud layers. The algorithm is based on the association between maxima of relative humidity and the presence of cloud layers. Relationships between cloud probability and relative humidity CP = f(RH) were developed that could be applied to sounding data to determine CP at each level.

A series of 19 raobs taken in varying cloud conditions and accompanied by copointing radar and lidar constituted the development data for the algorithm. The soundings were taken at Hanscom Air Force Base, Massachusetts, on various dates in July and August 2001 and June–August 2002. The 35-GHz AFCPR and the 1.574-μm PEELS measured reflectivity and backscattered power continuously during the raob flights. The AFCPR and PEELS time–height cross sections were used to determine the base and top altitude of each observed cloud layer. The higher of the radar or lidar top and the lower of the radar or lidar base was used in each case. In several of the soundings multiple cloud layers were present.

Relative humidity with respect to ice saturation (RH_i) was computed at each sounding level in which $T < 0$°C from measured P, T, and RH. Relative humidity used in developing the relationships for CP was set to measured RH (RH_l, assuming saturation vapor pressure with respect to a liquid surface) at levels where $T \geq 0$°C, computed RH_i where $T \leq -40$°C, and a temperature-weighted average of RH_l and RH_i where $0°C > T > -40°C$ [$RH = w \times RH_l + (1 - w) \times RH_i$, $w = (T/40) + 1$]. Then separate relationships of the form $CP = (a_0 \times a_1^{RH} + a_2)^{-1}$ were created for each temperature regime using a curve-fitting algorithm in the process described next.

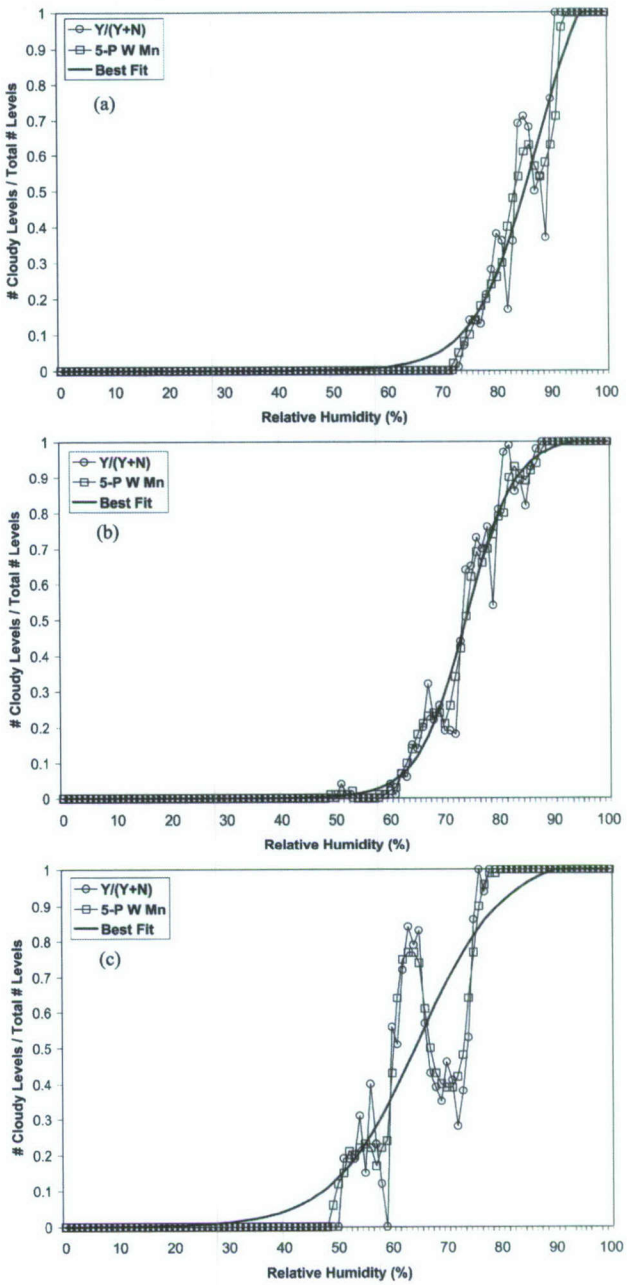

FIG. A1. Ratio of number of cloudy report levels to total number of report levels [$Y/(Y + N)$] for each 1% RH bin, its five-point weighted mean (5-P W Mn), and the nonlinear least squares best fit to the weighted mean (Best Fit) based on 19 collocated radiosonde observations and radar–lidar measurements of cloud layers from various dates in 2001 and 2002 taken at Hanscom Air Force Base, MA. Plots are shown for three different temperature regimes: (a) $T \geq 0$°C, (b) $0°C > T > -40°C$, and (c) $T \leq -40$°C.

Each sounding and the corresponding radar–lidar measurements of CTA and CBA are matched. We selected the measured CBA and CTA at the estimated times when a vertically pointing radar or lidar observes

TABLE A1. Coefficients of the nonlinear best fit to CP = $(a_0 \times a_1^{RH} + a_2)^{-1}$ derived from the 19 radiosonde soundings and corresponding radar–lidar cloud-base and cloud-top altitude measurements taken in 2001 and 2002 at Hanscom Air Force Base, MA. Coefficients are derived separately for the three temperature ranges shown in the table.

Temperature range	a_0	a_1	a_2
$T \geq 0$°C	$3.202\,991 \times 10^6$	$8.404\,975 \times 10^{-1}$	$7.947\,287 \times 10^{-1}$
0°C > T > −40°C	$1.2\,685\,548 \times 10^7$	$8.017\,294 \times 10^{-1}$	$9.877\,875 \times 10^{-1}$
$T \leq -40$°C	$3.670\,042 \times 10^3$	$8.805\,682 \times 10^{-1}$	$9.612\,840 \times 10^{-1}$

a cloud segment through which the sonde enters and exits after launch from the same ground site. This technique attempts to account for the downwind drift of the sonde from the time of its launch to the times it reaches cloud-base and cloud-top altitude. CBA and CTA estimates are then "fine tuned" by comparing them with the development RH values to place them where abrupt changes in the sounding are apparent near the estimated CBA and CTA levels. A value of CP = 1 is set for all sonde report levels lying between or at CBA and CTA for all cloud layers observed by the radar–lidar, and CP = 0 elsewhere.

All of the development RH and CP pairs at all levels in all of the soundings are binned by temperature regime, except for those levels within 500 m of the ground or above the tropopause (unless CP = 1 for the latter case) as determined by the algorithm of Roe and Jasperson (1980). For each temperature regime, the total number of report levels are counted (NRHT) for each integer value of development RH (0%–100%), and the number of report levels with CP = 1 are also counted (NRHC) for each 1% RH bin. Then for each development 1% RH bin, the probability of cloud occurring for that RH is CP_Ratio = NRHC/NRHT. A five-point weighted running mean (CP_FPRM) is computed for each 1% RH bin from the CP_Ratio values. The values of CP_FPRM are plotted versus their bin RH value. The value of RH for CP = 0.1 designated RHP and for the turning point CP = 0.5 designated RHT are picked off the curve for each temperature regime. Then in the regression equation CP = $(a_0 \times a_1^{RH} + a_2)^{-1}$ set $a_2 = 1$ (the simple logistic regression $[1 + \exp(b_0 + b_1 RH)]^{-1}$ where $a_0 = \exp(b_0)$ and $a_1 = \exp(b_1)$; see Wilks 1995) and solve for first guess values of a_0 and a_1 using the pair (CP = 0.1, RHP) and the pair (CP = 0.5, RHT). The 1% RH bins and their computed CP_FPRM values were submitted to a curve-fitting regression algorithm to determine the least squares best-fit values of a_0, a_1, and a_2 given their first-guess values. The best-fit relationship (CP_BF) was superimposed over the CP_Ratio and CP_FPRM curves and is shown in Fig. A1. Unlike logistic regression in which CP is guaranteed to lie within the range [0, 1], the three-parameter regression is not strictly limited to this range. So CP_BF values were restricted to the [0, 1] range in the plots.

Table A1 gives the least squares best-fit values of a_0, a_1, and a_2 for the regression equation CP = $(a_0 \times a_1^{RH} + a_2)^{-1}$ derived from the development soundings and corresponding radar–lidar cloud-base and cloud-top altitude measurements as described above. These values are used in the regression equation applied to the raobs discussed in the accompanying article. For the temperature ranges 5°C > T > −5°C and −35°C > T > −45°C, CP values assigned are temperature-weighted averages of the diagnosed CP values from the respective temperature regimes on either side of 0°C and −40°C boundaries. This insures a smooth transition of the CP values between temperature regimes. Diagnosed values of CP at each report level are then examined, and values of CP ≥ 0.51 are assumed to denote a cloudy level in the sounding. In this way, cloud-top and cloud-base altitudes are determined for each diagnosed cloud layer.

REFERENCES

Anderson, G. P., S. A. Clough, F. X. Kneizys, J. H. Chetwynd, and E. P. Shettle, 1986: AFGL atmospheric constituent profiles (0–120 km). Environmental Research Paper 954, AFGL-TR-86-0110, Air Force Geophysics Laboratory, 43 pp. [NTIS ADA 175173.]

Barton, D. K., and Coauthors, 2004: Report of the American Physical Society Study Group on boost-phase intercept systems for national missile defense: Scientific and technical issues. *Rev. Mod. Phys.*, **76,** S1–S424. [Available online at http://link.aps.org/abstract/RMP/v76/pS1.]

Bohren, C. F., and D. R. Huffman, 1983: *Absorption and Scattering of Light by Small Particles.* John Wiley and Sons, 530 pp.

Chernykh, I. V., and R. E. Eskridge, 1996: Determination of cloud amount and level from radiosonde soundings. *J. Appl. Meteor.*, **35,** 1362–1369.

Clough, S. A., F. X. Kneizys, E. P. Shettle, and G. P. Anderson, 1986: Atmospheric radiance and transmittance: FASCOD2. Preprints, *Sixth Conf. on Atmospheric Radiation,* Williamsburg, VA, Amer. Meteor. Soc., 141–144.

Comstock, J. M., and Coauthors, 2007: An intercomparison of microphysical retrieval algorithms for upper-tropospheric ice clouds. *Bull. Amer. Meteor. Soc.*, **88,** 191–204.

Desrochers, P. R., 2004: Cloud optical depth retrieval from cloud radar and microwave radiometer measurements. Environ-

mental Research Paper 1259, AFRL-VS-HA-TR-2004-1193, Air Force Research Laboratory, 21 pp. [NTIS ADA 443401.]

Donovan, D. P., and A. C. A. P. van Lammeren, 2001: Cloud effective particle size and water content profile retrievals using combined lidar and radar observations. 1. Theory and examples. *J. Geophys. Res.*, **106,** 27 425–27 448.

Fischer, K. W., M. R. Witiw, J. A. Baars, and T. R. Oke, 2004: Atmospheric laser communication: New challenges for applied meteorology. *Bull. Amer. Meteor. Soc.*, **85,** 725–732.

Fu, Q., 1996: An accurate parameterization of the solar radiative properties of cirrus clouds for climate models. *J. Climate,* **9,** 2058–2082.

Gustafson, G. B., and R. P. d'Entremont, 2000: Development and validation of improved techniques for cloud property retrieval from environmental satellites. Final Rep., AFRL-VS-TR-2001-1549, Air Force Research Laboratory, 48 pp. [NTIS ADA 395640.]

Kneizys, F. X., E. P. Shettle, L. W. Abreu, J. H. Chetwynd, G. P. Anderson, W. O. Gallery, J. E. A. Selby, and S. A. Clough, 1988: User's guide to LOWTRAN 7. Environmental Research Paper 1010, AFGL-TR-88-0177, Air Force Geophysics Laboratory, 137 pp. [NTIS ADA 206773.]

Koenig, G. G., D. R. Longtin, and J. R. Hummel, 1993: A study of the impact of cirrus clouds on high altitude, long horizontal path laser transmission. Scientific Rep. 7, PL-TR-93-2263, Phillips Laboratory, 30 pp. [NTIS ADA 278563.]

Liou, K. N., Y. Takano, S. C. Ou, and M. W. Johnson, 2000: Laser transmission through thin cirrus clouds. *Appl. Opt.*, **39,** 4886–4894.

McFarquhar, G. M., and A. J. Heymsfield, 1998: The definition and significance of an effective radius for ice clouds. *J. Atmos. Sci.*, **55,** 2039–2052.

Ou, S.-C., Y. Takano, K.-N. Liou, R. J. Lefevre, and M. W. Johnson, 2002: Laser transmission-backscattering through inhomogeneous cirrus clouds. *Appl. Opt.*, **41,** 5744–5754.

Roe, J. M., and W. H. Jasperson, 1980: A new tropopause definition from simultaneous ozone-temperature profiles. Interim Tech. Rep. 1, AFGL-TR-80-0289, Air Force Geophysics Laboratory, 16 pp. [NTIS ADA 091718; available from Donald C. Norquist, AFRL/RVBXS, 29 Randolph Rd., Hanscom AFB, MA 01731-3010.]

Seidel, D. J., and I. Durre, 2003: Comments on "Trends in low and high cloud boundaries and errors in height determination of cloud boundaries." *Bull. Amer. Meteor. Soc.*, **84,** 237–240.

Takano, Y., and K.-N. Liou, 1989: Solar radiative transfer in cirrus clouds. Part II: Theory and computation of multiple scattering in an anisotropic medium. *J. Atmos. Sci.*, **46,** 20–36.

Wang, J., and W. B. Rossow, 1995: Determination of cloud vertical structure from upper-air observations. *J. Appl. Meteor.*, **34,** 2243–2258.

Wilks, D. S., 1995: *Statistical Methods in the Atmospheric Sciences.* Academic Press, 467 pp.

Wylie, D. P., and W. P. Menzel, 1999: Eight years of high cloud statistics using HIRS. *J. Climate,* **12,** 170–184.